IRWIN AND JOAN JACOBS
CENTER FOR COMMUNICATION AND INFORMATION TECHNOLOGIES

Local and Global Fractal Behaviour in Mammographic Images

Ido Zachevsky and Yehoshua Y. Zeevi

CCIT Report #872
December 2014

DEPARTMENT OF ELECTRICAL ENGINEERING
TECHNION - ISRAEL INSTITUTE OF TECHNOLOGY, HAIFA 32000, ISRAEL

CCIT Report #872 December 2014

Local and Global Fractal Behaviour in Mammographic Images

Ido Zachevsky and Yehoshua Y. Zeevi
Technion, Israel Institute of Technology
Haifa, 32000, Israel
ido@tx.technion.ac.il, zeevi@ee.technion.ac.il

December 2, 2014

Abstract

Breast cancer is one of the leading causes of cancer in women. Most studies attempt to perform segmentation of tumors highlighted in mammogaphic images, or analysis of the contours of tumors for classification purposes. Successful segmentation and classification of tumors can assist physicians in revealing suspicious regions or masses, or differentiating malignant from benign tumors in the mammogram. However, relevant studies do not focus on the tumor surface statistics for the purpose of clustering or classification. In this work, we present a statistical, fractal-based approach, for the analysis of annotated tumors, reduced from the DDSM database. Using local and global fractal properties, obtained from the tumor surface, we show that malignant and benign tumors from are separable in an appropriate feature space. K-means-based clustering is performed, showing the efficacy of the method.

1 Introduction

Breast cancer is the most common cancer among women, and the second leading cause of cancer death in the general population [1]. Subsequent to the introduction of digital mammography, computer aided detection (CAD) methods have been extensively developed and used for various purposes, including classification of types of breast tissue highlighting suspicious regions and enhancement of calcifications.

Most of the classification-based approaches extract statistical information that is later fed to a classifier such as support vector machines (SVM) or k-nearest neighbours (kNN) [1–3]. Many such methods use texture-based or fractal-based properties for characterization of either segmented regions or complete tissues. These methods classify tissue properties related to density or fat, as these have been linked to existence of tumors in tissues [4, 5].

In this work, we attempt to differentiate malignant and benign tissue by local and global fractal properties. Rather than analysis for various properties such as

density of tissue, we use the features directly. We assume that segmentation of tumors can be performed, and our baseline data consists of high quality images of annotated tumors.

Random fields, and specifically, fractal random fields, have been extensively used for analysis of mammograms. In [6], Markov random fields have been used for classification of dense tissues. In [7], the fractional Brownian motion process (described hereinafter) has been proposed to model mammograms. In [8], fractal properties have been proposed for texture characterization. Classification has been performed in [9, 10]. In [11], high classification rates were obtained, based on data from radiologists. Autoregressive-moving average processes have also been used for mammography modelling [12]. A recent work has performed classification of malignant versus normal mammograms by fractal analysis performed on the background tissue [13].

The rest of the report is organized as follows. In Section 2, the background required for the understanding of the paper is presented. In Section 3, the data acquisition method is described, in Section 4 the statistical features extracted from the images are described, and in Section 5 the clustering results are presented.

2 Preliminaries

2.1 Stochastic fractal models

Fractal properties (scale invariance) are found in many natural images and phenomena [14]. Fractal analysis has been used on medical images as well, where in the case of mammography images, it has mostly been exploited on the curvature of the tumor boundary [15–18], but recent studies have also exploited 2D surfaces [13], showing that tumor shapes can be used for detection of malignant tissue [19].

2.1.1 Fractional Brownian motion (fBm)

FBm is a well-known fractal process, widely used in the context of analysis of natural images, including mammograms [20, 21]. FBm is a self-similar Gaussian random process, which was introduced by Mandelbrot and Van-Ness as a model suitable for natural images [22]. The fBm generalizes the well-known Brownian motion in that the increments are stationary but not independent. It is defined, in one dimension, as a Gaussian process with zero mean and the following autocorrelation function:

$$E\left[B_H(t)B_H(s)\right] = \frac{\sigma^2}{2}\left(|t|^{2H} + |s|^{2H} - |t-s|^{2H}\right), \tag{1}$$

where

$$\sigma^2 = \frac{\sigma_W^2}{2}\frac{\cos(\pi H)}{\pi H}\Gamma(1-2H), \tag{2}$$

σ_W^2 is a known variance, and the Hurst parameter, $H \in (0,1)$, characterizes the regularity of the process. Lower values of H correspond to rougher signals, and higher values of H correspond to smoother signals. Statistically, the process exhibits negative correlation between samples (anti-persistence) for $H \in \left(0, \frac{1}{2}\right)$, and positive correlation between samples for $H \in \left(\frac{1}{2}, 1\right)$. A special case is $H = \frac{1}{2}$, for which this process becomes the well-known Brownian motion, or Wiener process.

This process exhibits two important properties, known to characterize natural images, in the context of Mandelbrot's work on fractals [22]. The first one is long-range dependencies between samples, where for $H > 0.5$ the sum of the correlations of the increments diverges. The second property of the fBm, is its fractal (self-similarity) property:

$$B_H(at) \stackrel{d}{=} |a|^H B_H(t), \tag{3}$$

for a positive number a, where the equality is in distribution. This equality indicates that the sample distribution across different scales is varied only by a constant depending on the scale, a, and the Hurst parameter. These two properties highlight the relevance of this process to natural textures, as the latter often exhibit similarities between adjacent as well as distant pixels.

The fBm can be extended to two dimensions, and be used as a model for mammograms. However, the process is isotropic and governed by a single parameter, H, and it is, therefore, not suitable for proper characterization of mammographies, which have been shown to be anisotropic [20].

2.1.2 Extensions for multiple fractal dimensions

More complex fractal models have been proposed to better characterize fractal surfaces which do not have a single fractal dimension. One such model is the multifractional Brownian motion (mBm [23]), which assumes a time (or space in 2D) varying fractal dimension. It is obtained by extending the H of fBm to $H(t)$. Its corresponding covariance function (in 1D) is then:

$$E\left[B_H(t)B_H(s)\right] \propto |t|^{H(t)+H(s)} + |s|^{H(t)+H(s)} - |t-s|^{H(t)+H(s)}. \tag{4}$$

A different approach for complex fractal models was presented in the piecewise-fractional Brownian motion (pfBm), which assumes two different Hurst parameters, one for the lower scales and one for the higher scales [24]. It is derived from the spectral definition of the fBm, given by [25]:

$$B_H(t) = \frac{1}{2\pi} \int_{-\infty}^{\infty} F(\omega) \left(e^{jt\omega} - 1\right) d\beta(\omega), \tag{5}$$

where $\beta(\omega)$ is complex Brownian motion in frequency, and $F(\omega) = (j\omega)^{-(H+0.5)}$. The pfBm is obtained by using a different $F(\omega)$, specifically:

$$F(\omega) = \begin{cases} (j\omega)^{-(H_0+0.5)}, & 0 < |\omega| < \gamma \\ \gamma^{H_1-H_0}(j\omega)^{-(H_1+0.5)}, & \gamma \leq |\omega| < \infty. \end{cases} \quad (6)$$

The resulting random process has two frequency regions, with cutoff frequency γ, and two H parameters, H_0 and H_1. Therefore, the expected variance-scale behaviour is piecewise-linear with two distinct slopes.

2.2 Estimation of fractal dimensions

One of the most common methods for fractal dimension estimation is observation of the variance of wavelet coefficients across scales [26,27]. In true fractal surfaces, the decay of wavelet coefficient variance is proportional to $2^{j(2H+2)}$ for a given wavelet scale j. This power law property dictates a linear decay in log scale, where the slope of the decay curve corresponds to the fractal dimension. In the case of fBm, H corresponds to the fractal dimension. For more complex processes, such as the aforementioned mBm and pfBm, estimation is more elaborate as the processes are not governed by a single fractal dimension.

In 2D mBm, $H(x, y)$ is a spatial function, that cannot be practically estimated for a general function, given a limited set of images. Instead, one can propose parametric $H(x, y)$, or coarser functions, where the fractal dimension is piecewise constant for small patches. This is the approach we adopt in the present study, where we estimate patch-wise fractal dimensions. For pfBm, one has to estimate the two H parameters, H_0 and H_1, for the different scales, as well as the cutoff frequency, γ (Eq. (6)).

2.3 Principal Component Analysis (PCA)

PCA is a well-known method for dimensionality reduction and clustering [28]. The application of PCA results in a transform that projects the given data to a space in which its variability (variance) is maximized. This yields a more efficient representation, that minimizes the mean-squared error (MSE) obtained in reconstruction by a given, predetermined number of basis vectors. For a centered matrix $X \in \mathbb{R}^{n\times d}$, of n samples with d features per sample, the principal components are the sample covariance matrix eigenvectors corresponding to the highest eigenvalues. The sample covariance matrix, for a centralized data matrix X, is given by:

$$\Sigma = XX^T. \quad (7)$$

PCA works well for clustering purposes on linearly separable samples. If the samples are not linearly separable, it can be extended using kernel methods [28], by first projecting each sample, $x \in \mathbb{R}^d$, to a higher dimensional space by a known mapping $\phi : \mathbb{R}^d \to \mathbb{R}^N$, where $N > d$. The resulting kernel-PCA first projects the data onto a higher (possibly infinite) dimensional space by calculating $\phi(x)$,

and then performs PCA in this feature space, in which the transformed data are expected to be linearly separable.

Kernel-PCA can be performed efficiently due to what is known as the "kernel trick", where all the calculations are performed in the original space, rather than the higher dimensional space. The kernel trick is possible since all data calculations in kernel-PCA are expressed via the inner product xx^T, which corresponds to $\phi^T(x)\phi(x)$ in the feature space. Therefore, by first constructing a kernel matrix, $K(x,y)$, containing all combinations of $\phi^T(x)\phi(y)$, no calculation in the high dimension is required.

The kernel function, $K(x,y)$, describes the method in which the data are transformed to the feature space. Common kernel functions are order r polynomial, $K(x,y) = (x^T y+1)^r$, and radial basis function (RBF), $K(x,y) = \exp\left(-\frac{1}{2\sigma^2}(x-y)^2\right)$, with a given width σ. The latter, used in this study, assigns high values for close samples, and acts as an inverse distance function. Thus, the kernel-PCA tends to group close samples in the feature space.

Recently, more advanced methods have been proposed, which attempt to better represent high dimensional data on a lower dimensional manifold [29, 30]. These methods have some advantages over PCA and, possibly, over kernel-PCA.

3 Data acquisition

The tumor images were extracted from the Digital Database for Screening Mammography (DDSM) [31]. The raw data contains images in raw lossless-JPEG format (LJPEG), as well as annotation and biopsy-confirmed pathology information indicated by medical experts, which served as the ground truth for this study. The images were first converted to PNG and the circumscribed rectangle (bounding box) of each tumor was extracted, to be used as the data for this study. Depending on the type of feature, either the entire bounding box content was analyzed, or only the tumor interior.

This study is concerned with malignant/benign tumors. Therefore, any images of normal tissues (from the `normal_NN` volumes) were discarded. Further, images containing only micro-calcifications, were discarded as well and were not considered in this study. This is due to the fact that their statistical properties are different than tumors, despite their connection to cancer prediction. The final database contained 524 images, with binary labels corresponding to malignant or benign. Due to the various sizes of tumors, the sizes of the bounding boxes had a large variance as well, where the smallest was of size 137×137 pixels, and the largest contained 3153×1720 pixels.

One of the contributors to successful clustering and analysis of tumors is the high resolution of the DDSM images. Using other databases, such as the Mini-MIAS database which contains smaller versions of size 1024×1024 pixels per image, would produce significantly lower resolution of the tumors, which only occupy a

relatively small area of the mammogram.

4 Statistical features

The emerging model suitable for the tumor images is fractal, with local fractal properties, corresponding to space-varying H. Therefore, the mBm is a suitable model. However, there also exists global fractal behaviour, albeit too complex to be described by a single fractal dimension (in the case of fBm) or two fractal dimensions in different scales (in the case of pfBm), as we demonstrate hereinafter. For this reason, we perform both local estimation of the H parameters, and parametric global estimation for the decay of wavelet coefficient variance over scales.

4.1 Global features

Global assessment was performed for each tumor image. First, each image was upscaled to the size of the highest dimensional tumor image. This stage may produce artefacts, but was shown to be superior to the alternative of using original size tumors, which produce significant differences between tumors of different sizes.

Each tumor image was decomposed by using both Coifman-2 and Coifman-5 wavelets [26], and their variance-scale curves were analyzed. Although visual assessment of the tumors may lead to the conclusion they are fractal in the usual sense, i.e. with a single fractal dimension, their accurate analysis yield more complex properties. The natural model for more complex fractal features in frequency, as is this case, is the pfBm. This process depicts a variance-scale plot of two distinct slopes, that are indeed characteristic of some of the encountered images. However, due to the delicate difference between benign and malignant tumors, the three parameters were not found to be selective (Fig. 1).

Instead of using a known fractal model for analyzing this behaviour, we extracted the parameters of the variance-space curve itself. The two distinct properties of the observed curve were a negative trend, and an oscillating, sine-like, behaviour. The curve function was estimated as follows. First, the trend was estimated using a first-order polynomial curve fitting, to yield the line (p_1, p_2). Then, the following function was fitted:

$$f(x) = c + d \cdot M_{2,1} \cdot x + b \cdot M_{2,2} \cdot \sin(ax - e), \tag{8}$$

where (a, b, c, d, e) are the fit parameters, and M is a rotation matrix with angle θ, derived from the slope of the fitted trend. This fit yields a vector of 7 parameters: $(p_1, p_2, a, b, c, d, e)$ for wavelet family.

In addition to this analysis, the same function was fitted to the derivatives in the x and y directions of each tumor image, thus yielding 28 global features.

Examples illustrating the goodness of fit are depicted in Fig. 2. This function can be further optimized, but it shows overall good behaviour. This expresses the

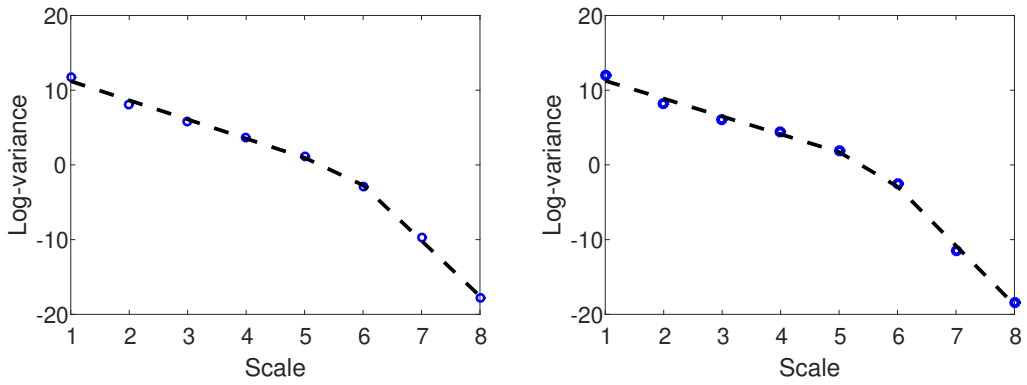

(a) Coifman-2

(b) Coifman-5

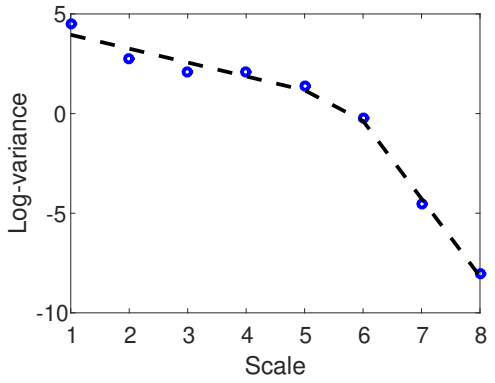

(c) x-direction Coifman-2

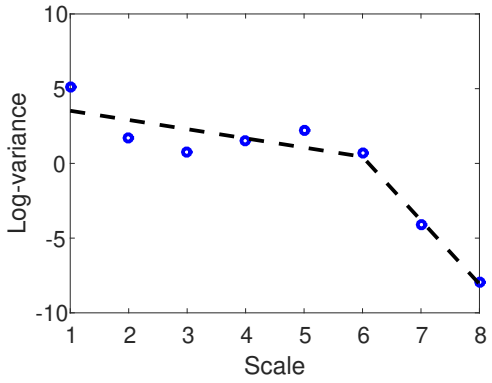

(d) y-direction Coifman-2

Figure 1: Example of a characteristic image with pfBm parameters: piecewise linear fit with a single cutoff point. While the fit yields moderately low error, it can still be further improved. Each figure shows the true log-variance measurements (blue circles) and the fitted function (dashed black).

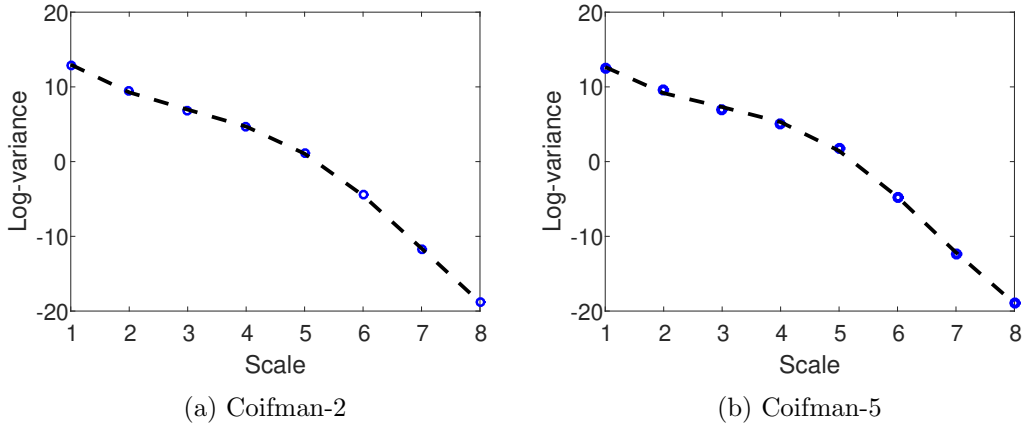

(a) Coifman-2

(b) Coifman-5

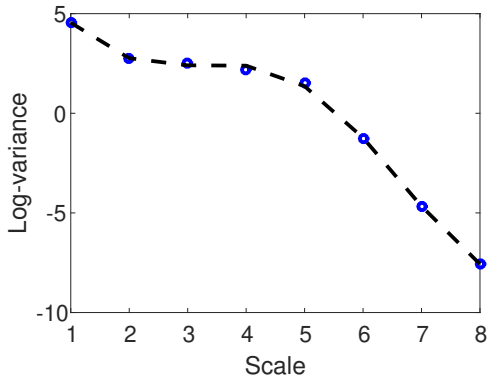

(c) x-direction Coifman-2

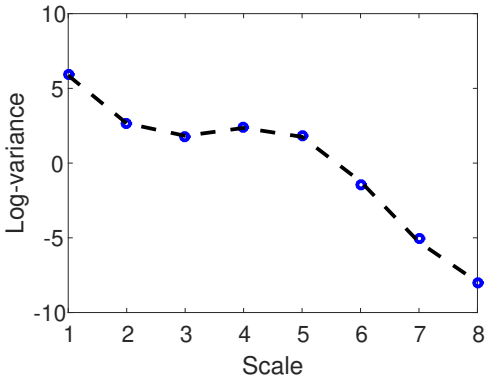

(d) y-direction Coifman-2

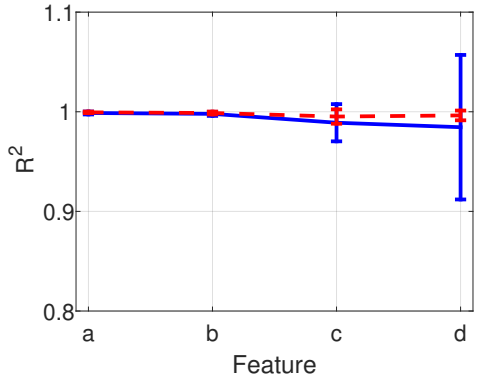

(e)

Figure 2: Example of a single, characteristic, patch. The general behavior of the variance decay is not a straight line, as expected from a fractal surface with a single fractal dimension. Each figure shows the true log-variance measurements (blue circles) and the fitted function (dashed black). The R^2 fit values are depicted in Fig. (e), displaying a good fit with R^2 values close to 1. The cancer and benign fits are depicted in blue and dashed red respectively. It is also apparent that the R^2 standard deviations are different for the x- and y-directional fits, which may indicate a difference between the two classes.

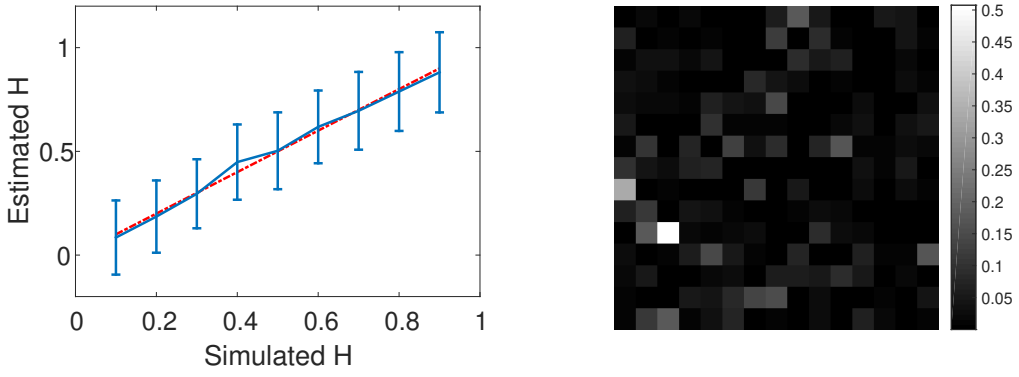

(a) (b)

Figure 3: Hurst (H) parameter estimation based on 16×16-sized patches. (a) True versus estimated H parameters for a 256×256 images: an isotropic fBm image was synthesized for each value of H, and its value was then estimated for each small patch. The mean (blue line) and standard deviation (error bars) for each H value are displayed, as well as the true value (dashed red). (b) An example of a single image estimation error: a 256×256 image with $H = 0.5$ was synthesized, and its H-value pixel-wise squared error was calculated. Most of the values are close to zero.

nature of the fractal behaviour of the mammographic images, which is more complex than a single or even two fractal dimensions.

4.2 Local features

Each annotated tumor is divided into 16×16-sized non-overlapping patches, from which isotropic and anisotropic Hurst parameters are extracted. Studies [32, 33], as well as our experiments, show that this patch-size is large enough for estimation of Hurst parameters. To evaluate the performance of the local H estimator, we simulated 2D fBm images, with known Hurst parameters, and attempted to estimate their value (Fig. 3).

Each estimation was performed in the wavelet domain, using Coifman-2 wavelets. The patch was first upscaled by bicubic interpolation to 64×64, and later decomposed to 7 levels. The Hurst parameter, H, was estimated via the slope of the variance-scale curve, similarly to known fractal dimension estimation methods [34].

Each patch yielded three values of H: (H, H_x, H_y). H was obtained via the patch itself, and H_x and H_y were obtained by evaluating the Hurst parameter on the derivatives in the x and y directions respectively. Inasmuch as the annotated tumor images have, in general, non rectangular shape, only patches with over 80% tumor content were included.

As the patch sizes vary, a standard measurement was incorporated to properly produce uniform features for each patch. Therefore, the following statistical features were evaluated, for each Hurst parameter and each patch: mean, variance, kurtosis and skewness, as characteristic features for the distribution of the local parameters. The number of local features was, therefore, 12.

5 Clustering

The main goal for mammography tumors is performing classification, using geometric and statistical features. However, as a preliminary problem, we attempted to perform clustering. Clustering was performed using the entire features' vector (40 features) per sample, with the annotated tumors.

Kernel-PCA with radial basis functions (RBF) was chosen for clustering. This method was preferred due to the non-linearity of the data structure, requiring a higher dimensional space for proper separation between malignant and benign samples.

The kernel-PCA implementing RBF required a single parameter - the width of the Gaussian-shaped kernel function, σ. Due to the expected small distance (in the feature space) between the malignant and benign samples, it was determined to be small, at $\sigma = 10^{-6}$. Kernel-PCA performs PCA on the kernel matrix, which, therefore, produces as many principal components as the number of samples. Correct selection of principal components is therefore crucial, and was performed as follows: a training set of 100 samples was selected, having an equal number of benign and malignant tumors. Then, the eigenvalues of the kernel matrix were calculated twice: once for each set of tumors. Using the resultant two vectors, 20 principal component indices were chosen, corresponding to the eigenvalues that maximize the difference between the two sets.

The results obtained by using the kernel-PCA which incorporates the chosen principal components yields a significant difference between the two classes. These results can be classified via k-means clustering, as will be performed hereinafter. However, out of the 535 samples in the dataset, large variance deviations were encountered in the principal component values; 211 samples' components had energy lower than 10^{-7}, whereas the rest of the samples had values in the range of $0.1 - 1.0$. Therefore, the small-variance benign and cancerous samples were mapped very close to the origin.

In order to better classify the low-variance samples, they were extracted from the first PCA, and kernel-PCA was performed for these samples separately. Due to the very low variance, a logarithmic function was applied:

$$f(x) = \log(10^{-8} + |x|). \tag{9}$$

The data was, therefore, separated into two sets, A and B, where the former had relatively high variance, and the latter had low variance. By this division, good clus-

tering results could be obtained, as the data were separated by a proper clustering algorithm (Fig. 4).

K-means algorithm [28] was evaluated on both A and B, with RBF kernel, and kernel width of 0.01 (Fig. 5). The clustering errors were 4.9% and 30.8% for A and B respectively. Incorporating the number of samples per set, the final clustering error was 15.1%. Due to the fact that K-means does not identify each class, the correct class assignment was assumed. This can be based, for instance, on knowledge of a single true classification per set. The two different sets, A and B, should be further investigated to recover the underlying properties that yield the observed difference in variance.

6 Discussion

This preliminary study shows that both local and global fractal properties are important ingredients in characterizing tumor image structure, with reference to their diagnosis as malignant or benign. Once the results are further improved, classification will become a viable goal, that can contribute to a variety of other methods for such tasks, where the advantage of these methods is in being non-invasive.

The current study should eventually lend itself to characterization of tumors. If the features are indeed sufficient for differentiating different tumors, they can be used for image retrieval, where a given, unclassified, tumor may serve as a reference, and a dedicated algorithm can then find statistically similar tumors that were previously tagged, with their known diagnosis.

An underlying model for tumor images, emerging from this study, is a multiscale model, with statistical behaviour that locally corresponds to mBm, but yet has some global structure which generalizes the pfBm. Once such a field is constructed, better parameter estimation, and better understanding of the structure of tumors will be obtained.

Acknowledgements

This research program has been supported by the Technion Ollendorff Minerva Center for Vision and Image Sciences. Ido Zachevsky has been an Ollendorff Fellow.

The authors thank Prof. Dmitry Goldgof (USF) for making the image database available for our purposes.

References

[1] T. Subashini, V. Ramalingam, and S. Palanivel, "Automated assessment of breast tissue density in digital mammograms," *Comput. Vis. Image Underst.*, vol. 114, no. 1, pp. 33–43, Jan. 2010.

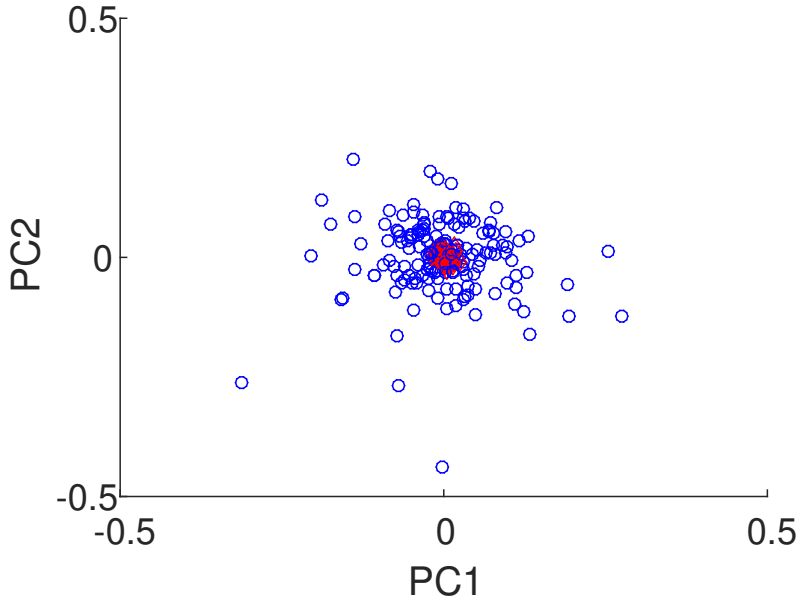

(a) Set A

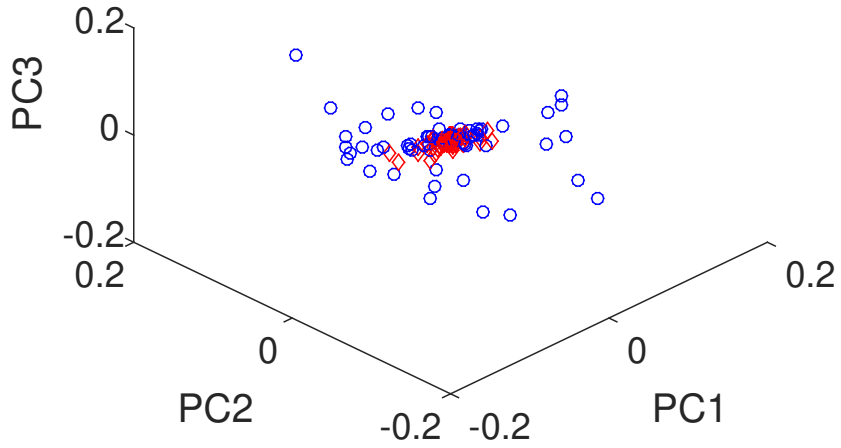

(b) Set B

Figure 4: Kernel-PCA results on sets A (high variance) and B (low variance). The malignant tumors (blue) show different characteristic scatter, different from that of the benign (red diamond). Kernel-PCA was performed on unlabeled samples, and the different colors were applied for visual assessment.

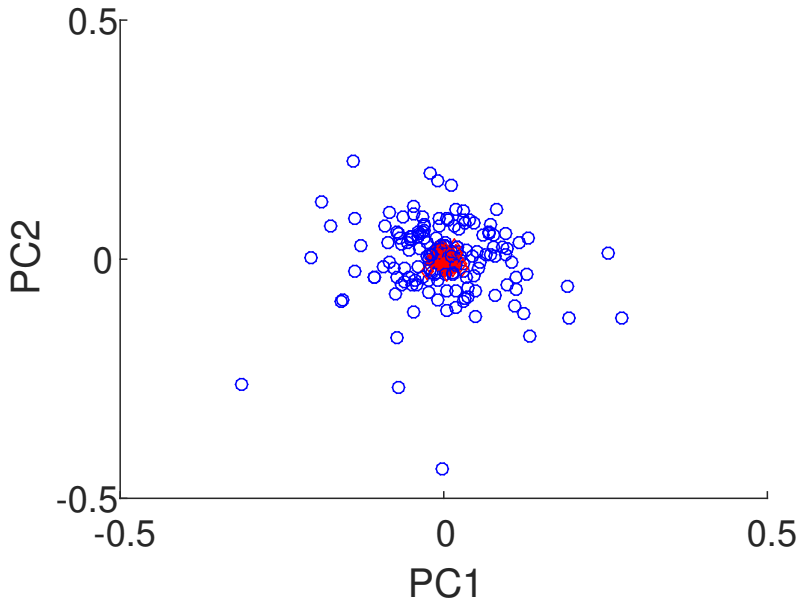

(a) Set A: 4.9% error.

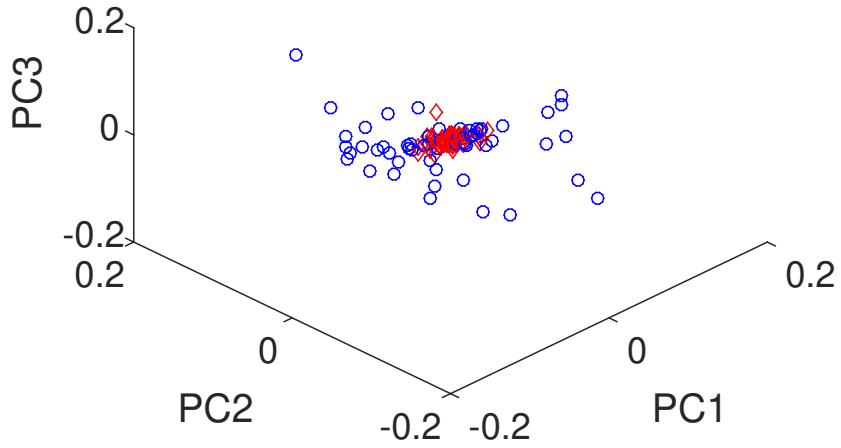

(b) Set B: 30.8% error.

Figure 5: K-means results on both sets. Notice the similarity to the ground truth (Fig. 4).

[2] G. Braz Junior, A. Cardoso de Paiva, A. Corrêa Silva, and A. Cesar Muniz de Oliveira, "Classification of breast tissues using Moran's index and Geary's coefficient as texture signatures and SVM." *Comput. Biol. Med.*, vol. 39, no. 12, pp. 1063–72, Dec. 2009.

[3] H. Cheng, X. Shi, R. Min, L. Hu, X. Cai, and H. Du, "Approaches for automated detection and classification of masses in mammograms," *Pattern Recognit.*, vol. 39, no. 4, pp. 646–668, Apr. 2006.

[4] V. a. McCormack and I. dos Santos Silva, "Breast density and parenchymal patterns as markers of breast cancer risk: a meta-analysis." *Cancer Epidemiol. Biomarkers Prev.*, vol. 15, no. 6, pp. 1159–69, Jun. 2006.

[5] J. N. Wolfe, "Breast patterns as an index of risk for developing breast cancer," *Am. J. Roentgenol.*, vol. 126, no. 6, pp. 1130–1137, 1976.

[6] Y. C. Gong, M. Brady, and S. Petroudi, "Texture based mammogram classification and Segmentation," pp. 616–625, 2006.

[7] G. Mcgarry, "Modelling mammographic images 'itsing fractional brownian motion," pp. 299–302, 1997.

[8] R. Lopes, P. Dubois, I. Bhouri, M. Bedoui, S. Maouche, and N. Betrouni, "Local fractal and multifractal features for volumic texture characterization," *Pattern Recognit.*, vol. 44, no. 8, pp. 1690–1697, Aug. 2011.

[9] R. Swiniarski, H. Lim, J. Shin, and A. Skowron, "Independent Component Analysis, Princpal Component Analysis and Rough Sets in Hybrid Mammogram Classification." *IPCV*, no. 1, 2006.

[10] O. Nicolis, S. Jeon, and B. Vidakovic, "Mammogram Diagnostics via 2D Complex Wavelet-based Self-similarity Measures," 2012.

[11] B. Verma, P. McLeod, and A. Klevansky, "Classification of benign and malignant patterns in digital mammograms for the diagnosis of breast cancer," *Expert Syst. Appl.*, vol. 37, no. 4, pp. 3344–3351, Apr. 2010.

[12] J. Zielinski and D. Schonfeld, "Two-Dimensional ARMA Modeling for Breast Cancer Detection and Classification," 2010.

[13] P. Ramírez-Cobo and B. Vidakovic, "A 2D wavelet-based multiscale approach with applications to the analysis of digital mammograms," *Comput. Stat. Data Anal.*, vol. 58, pp. 71–81, Feb. 2013.

[14] A. P. Pentland, "Fractal-based description of natural scenes." *IEEE Trans. Pattern Anal. Mach. Intell.*, vol. 6, no. 6, pp. 661–74, Jun. 1984.

[15] R. M. Rangayyan, N. M. El-Faramawy, J. E. Desautels, and O. a. Alim, "Measures of acutance and shape for classification of breast tumors." *IEEE Trans. Med. Imaging*, vol. 16, no. 6, pp. 799–810, Dec. 1997.

[16] R. M. Rangayyan, F. Oloumi, and T. M. Nguyen, "Fractal analysis of contours of breast masses in mammograms via the power spectra of their signatures." *Conf. Proc. IEEE Eng. Med. Biol. Soc.*, vol. 2010, pp. 6737–40, Jan. 2010.

[17] N. R. Mudigonda, R. M. Rangayyan, and J. E. Desautels, "Detection of breast masses in mammograms by density slicing and texture flow-field analysis." *IEEE Trans. Med. Imaging*, vol. 20, no. 12, pp. 1215–27, Dec. 2001.

[18] T. Nguyen and R. Rangayyan, "Shape Analysis of Breast Masses in Mammograms via the Fractal Dimension." *Conf. Proc. IEEE Eng. Med. Biol. Soc.*, vol. 3, pp. 3210–3, Jan. 2005.

[19] A. C. Sie, G. C. Hansen, J. S. Prince, M. L. Melany, H. E. Reynolds, V. P. Jackson, J. W. Sayre, and L. W. Bassett, "Benign versus Malignant Solid Breast Masses :," no. 13, pp. 889–894, 1999.

[20] F. Richard and H. Bierme, "Statistical Tests of Anisotropy for Fractional Brownian Textures. Application to Full-field Digital Mammography," *J. Math. Imaging Vis.*, vol. 36, no. 3, pp. 227–240, Dec. 2009.

[21] G. P. O. Box and B. Qld, "Microcalcification detection in mammographic images using fractional Brownian motion," pp. 1–3.

[22] B. B. Mandelbrot and J. W. Van Ness, "Fractional Brownian motions, fractional noises and applications," *SIAM Rev.*, vol. 10, no. 4, pp. 422–437, 1968.

[23] R. F. Peltier and J. Levy-vehel, "Multifractional Brownian motion: definition and preliminary results," Tech. Rep., 1995.

[24] E. Perrin, R. Harba, I. Iribarren, and R. Jennane, "Piecewise fractional Brownian motion," vol. 53, no. 3, pp. 1211–1215, 2005.

[25] I. Reed, P. Lee, and T. Truong, "Spectral representation of fractional Brownian motion in n dimensions and its properties," *IEEE Trans. Inf. Theory*, vol. 41, no. 5, pp. 1439 –1451, Sep. 1995.

[26] I. Daubechies and Others, *Ten lectures on wavelets*. SIAM, 1992, vol. 61.

[27] B. Pesquet-Popescu and J. L. Vehel, "Stochastic fractal models for image processing," *IEEE Signal Process. Mag.*, vol. 19, no. 5, pp. 48– 62, Sep. 2002.

[28] J. Beutel, J. M. Fitzpatrick, S. C. Horii, H. L. Kundel, and R. L. V. Metter, *Handbook of Medical Imaging: Volume 2. Medical Image Processing and Analysis.*

[29] S. T. Roweis and L. K. Saul, "Nonlinear dimensionality reduction by locally linear embedding." *Science*, vol. 290, no. 5500, pp. 2323–6, Dec. 2000.

[30] R. R. Coifman and S. Lafon, "Diffusion maps," *Appl. Comput. Harmon. Anal.*, vol. 21, no. 1, pp. 5–30, Jul. 2006.

[31] M. Heath, K. Bowyer, D. Kopans, R. Moore, and W. P. Kegelmeyer, *The Digital Database for Screening Mammography*. Medical Physics Publishing, 2001.

[32] U. Disturbances, "PCA Based Hurst Exponent Estimator for fBm Signals Under Disturbances," *IEEE Trans. Signal Process.*, vol. 57, no. 7, pp. 2840–2846, Jul. 2009.

[33] C. Nafornita, A. Isar, and J. Nelson, "Regularised, semi-local Hurst estimation via generalised lasso and dual-tree complex wavelets," in *Proc. IEEE Int. Conf. Image Process.*, 2014.

[34] C. Parra, K. Iftekharuddin, D. Rendon, and A. I.-d. Case, "Wavelet Based Estimation of the Fractal Dimension in fBm Images," no. 9, pp. 533–536, 2003.